ALGORITHMS FOR MAGNETIC FLUX LEAKAGE TESTING

AUSWERTUNGSALGORITHMEN FÜR DIE MAGNETISCHE STREUFELDMESSUNG

Jonathan Villing, Frank Lehmann, Michael Schreiner, Helmut Ernst

Materials Testing Institute (MPA), University of Stuttgart, Otto-Graf-Institute

SUMMARY

The aim of the magnetic flux leakage test is the detection of fractures in prestressing steel in existing buildings. For this purpose, the prestressed concrete components are magnetized, and the magnetic stray field is measured. In the measured magnetic stray fields, prestressing steel fractures can be identified by the specific fracture shape in the measured magnetization curves. The greatest challenge in fracture detection is the suppression of interference signals, which are primarily triggered by the mild steel reinforcement (rebars). For this purpose, different evaluation algorithms were developed, which were investigated and evaluated on simplified test setups.

ZUSAMMENFASSUNG

Das Ziel der magnetischen Streufeldmessung ist die Detektion von Spannstahlbrüchen in Bestandsgebäuden. Dazu werden die Spannbetonbauteile magnetisiert und das magnetische Streufeld gemessen. In den gemessenen Magnetfeldern können Spannstahlbrüche durch die spezifische Bruchform in den gemessenen Magnetisierungskurven identifiziert werden. Die größte Herausforderung bei der Bruchdetektion ist die Unterdrückung von Störsignalen, die primär durch die schlaffe Betonstahlbewehrung (Bügel) ausgelöst werden. Zu diesem Zweck wurden unterschiedliche Auswertungsalgorithmen entwickelt, die an vereinfachten Versuchsaufbauten untersucht und bewertet wurden.

1. INTRODUCTION

Prestressed concrete makes it possible to build structures that span large distances with elegance, durability, and high structural strength. Almost 70 % of all bridges on German federal highways are therefore made of prestressed concrete. The building material is also used in many other engineering structures, such as sports halls, industrial buildings, event venues, railway stations and airports, trade fairs, theatres and many more.

The load-bearing capacity of prestressed concrete depends significantly on the condition of the tendons. If these fail, the stability of the structure can be compromised. As the steel is embedded in the concrete, visual inspection is not sufficient to reliably assess the condition.

In modern prestressed concrete, the tendons are reliably protected from corrosion and accidental mechanical damage by the surrounding concrete. However, prestressed concrete structures should be specifically inspected if any of the following risk factors apply:

- Tempered prestressing steels:

  Until 1993, some of the prestressing steels used were quenched and tempered steels which can fail suddenly (St 145/160, trade names Neptun and Sigma, and St 140/160, Hennigsdorfer prestressing steel). These carry the risk that failure may not be preceded by noticeable cracking on the concrete surface or signs of corrosion. Until the 1970s, little additional steel reinforcement was provided as it was assumed that prestressed concrete structures did not require it. As a result, force redistribution in the event of tendon failure is often limited.

  Information on the prestressing steel used can either be obtained from the design record or a section of the steel has to be tested in the laboratory.

- Corrosion:

  Poor corrosion protection and cracks accessible to water significantly increase the probability of failure of all prestressing steel grades. In particular, if chlorides (road salt, sea air) can penetrate the concrete with the water, and if cladding tubes are not fully grouted, there is a higher potential for damage.

When inspecting a structure, particular attention should be paid to water drainage marks, defective surface seals and evidence of existing corrosion damage such as rust staining, cracking or concrete spalling.

- Mechanical damage:

  Time and again, prestressed concrete girders are carelessly punctured in the area of the prestressing steel in order to attach structural elements to them. The inherently good protective properties of concrete do not help in this case.

- Fatigue and overloading:

  The ever-increasing traffic loads on infrastructure buildings can cause prestressed concrete to age prematurely compared to design. Coupling joints have historically been particularly critical in this regard. However, tendon damage can also be caused by isolated events such as static overloading, vehicle impact, fire, earthquakes, floods and extreme storm events.

- Alumina cement:

  In the years 1952 to 1963, the binder alumina cement was sometimes used in the construction of prestressed concrete elements. If the relative humidity in the area of the load-bearing structure permanently remains above 70 %, or if water can penetrate the prestressed concrete due to inadequate waterproofing, there is a risk of collapse. Damage to the prestressing wires can usually not be detected visually in advance. It is recommended that such structural systems be inspected with a magnetic flux leakage testing.

Owners, holders, operators, and other parties responsible for the construction of a prestressed concrete structure are legally obliged to ensure the structural stability of their buildings at all times. However, in order to preserve the value of the structure and to keep it in use, defects in the load-bearing structure should always be identified and repaired in good time.

The applicable codes of practice result in a statutory inspection requirement for every long-span superstructure. These include, among others, the bridge inspection according to DIN 1067, the regular structural inspection of buildings according to VDI 6200 and the inspection of railway bridges according to DB guideline 804.8002.

An additional inspection is recommended after exceptional events, alterations, changes of use or modernisation. If defects have already occurred, a property damage analysis should be carried out to assess stability.

2. MAGNETIC FLUX LEAKAGE TEST

The method of magnetic flux leakage testing used for the non-destructive and non-contact detection of fractures in the near-surface prestressing reinforcement of prestressed concrete. The test head, which contains a yoke magnet and magnetic field sensors, is moved along the prestressing reinforcement on a rail. The magnetic field of the yoke magnet generates a magnetisation in the prestressing reinforcement to be tested. At a fracture point, a magnetic leakage flux escapes, which is measured by the magnetic field sensors.

When reading the axial component of the magnetic field, the fracture is indicated as a local extreme value (maximum). This is shown schematically in Fig. 1. Due to the ferromagnetic behaviour of the prestressing steel, its magnetisation remains partially intact even after the magnetic field of the yoke magnet is switched off, allowing fractures to be detected as well through the measurement of the remanent field.

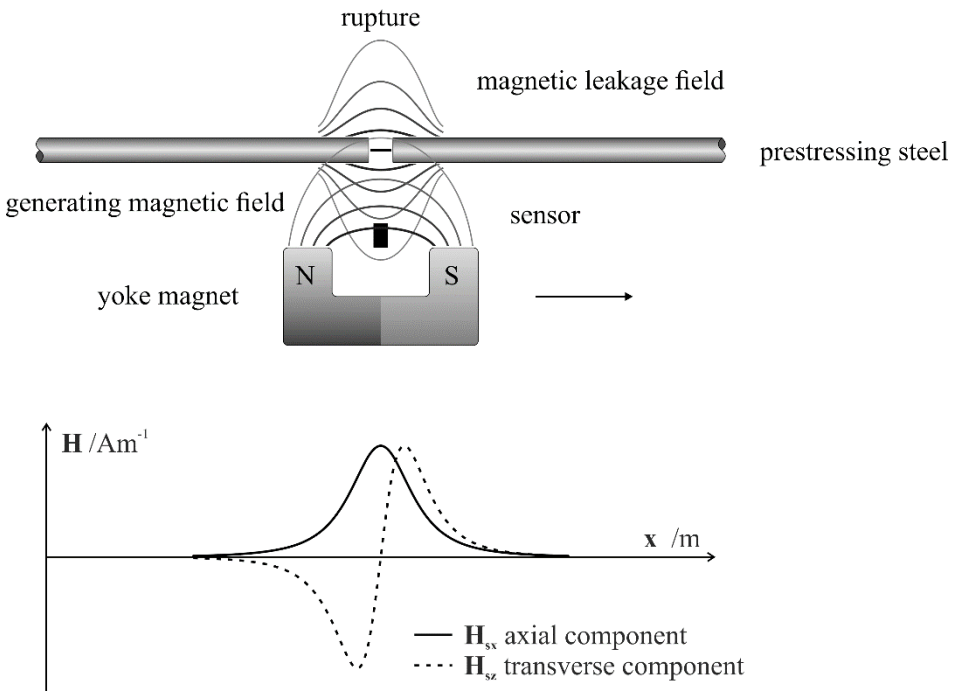

Fig. 1: Schematic representation of the axial and transverse components of the magnetic field strength at a prestressing steel fracture

In prestressed concrete components, slack rebars are also present in addition to the prestressed reinforcement. These contribute significantly to the magnetic stray field. To interpret the measured leakage field signals, the magnetic components of the slack reinforcement (mostly stirrup reinforcement transverse to the direction of travel) must be filtered out. In order to be able to achieve this optimally, several measurement passes are carried out with the test head, in which the magnetic field of the electromagnet features different field strengths in each case. The aim is to magnetise the tension reinforcement as evenly as possible and at the same time to demagnetise the slack reinforcement as far as possible.

During the inspection, measurements are carried out with active magnet (stray field measurements) and with inactive magnet (residual field measurements) at the same time. During measurements in the active field, the slack reinforcement near the surface emerges clearly in the data and can thus be effectively localised. The measurements with the yoke magnet switched off enable in particular the differentiation between hard magnetic and soft magnetic steel, i.e. between prestressing steel and slack reinforcement.

At the end of the test, when the slack reinforcement is already largely demagnetised, the signals of the cross bars are magnetically inverted by moderately magnetising the reinforcement on the reverse trip. The signals of the transverse bars then cancel each other out in the sum of the last two residual field measurements. In actual practice, this does not entirely occur, so that additional filtering is necessary. This is described in detail in section 3.

For the evaluation of the individual fracture signals, geometric factors have to be considered. Besides the mentioned test head distance to the prestressing steel, these are the fracture amplitude and the fracture orientation.

Up to a fracture width of approximately 1 mm, the fracture amplitude increases strongly and then approaches a limit value. At a fracture width of 0.5 mm, about 80 % of the maximum fracture amplitude is reached. In practice, fracture widths of approximately 1 to 2 mm occur.

Regarding the fracture orientation, the most favourable case for detection is when the fracture is facing the magnet. If the break occurs at the side of the tendon, the measured break amplitude is reduced to about half. In the worst case of a break facing away from the test head, the amplitude is reduced to about 40 %.

With constant fracture orientation, the fracture signal strength increases approximately linear with increasing cross-sectional reduction. This case occurs, for example, among prestressing steel bars and single-bar anchors. In prestressing steel strands, prestressing wires can be disconnected at different fracture orientations, inside the bundle or with a slight offset in the tendon direction (staggered fracture). Depending on the boundary conditions, cross-sectional weakening of up to 20 % can therefore occur, which do not lead to a fracture indicator in the evaluation and thus remain undetected. The detection limit is therefore assumed based on laboratory measurements with 20 % broken tension wires in a strand [1],[5].

3. ALGORITHMS FOR FRACTURE DETECTION

The signals of the magnetic flux leakage test are not only affected by rupture signals but mainly by the mild steel reinforcement (rebars) which are located at shorter distance to the probe than the prestressing steel. To suppress these unwanted signals several algorithms have been developed [2],[3],[4],[5],[6],[7]. First the methods and formulas are described and afterwards illustrated in an example. The example is based on the raw data shown in Fig. 2 and Fig. 3. To facilitate interpretation of the data, the key features of the setup are labelled. A detailed explanation of the structure will be given in chapter 5.

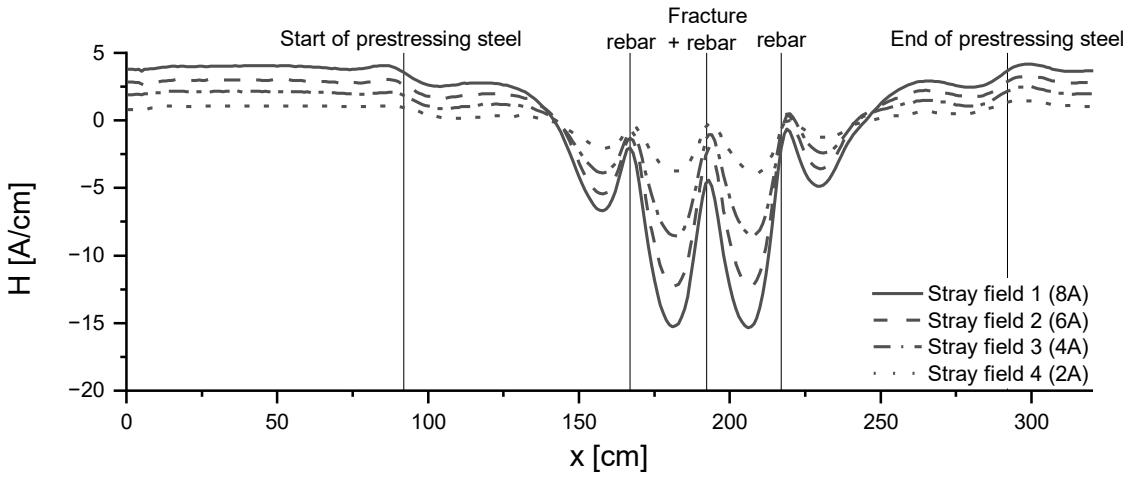

Fig. 2: Stray field measurements 1 (8 A), 2 (6 A), 3 (4 A) and 4 (2 A)

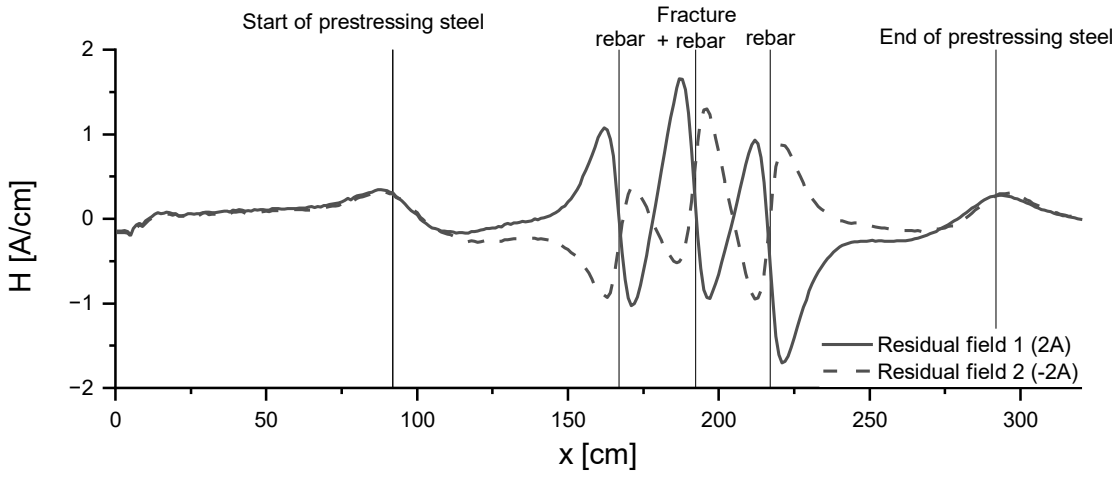

Fig. 3: Residual field measurements 1 (2 A) and 2 (-2 A)

3.1 Similarity function for active stray field measurements

The similarity function for active stray field measurements uses the ferromagnetic material behaviour of rebars and prestressing steel. When the magnetizing field strength is increased, the rebars reach saturation faster than the prestressing steel. After the rebars reach saturation, their signal changes only proportionally to the magnetizing field, while the fracture signals of the prestressing steel continue to increase. By comparing two measurements with different magnetising field strengths, the change in signal shape can indicate fracture.

$$r_{p1,p2} = \frac{\int_{-h}^{h} \left(H(p_{1,x}+t) - \overline{\mathrm{H}}(p_{1,x})\right) * \left(H(p_{2,x}+t) - \overline{\mathrm{H}}(p_{2,x})\right) dt}{\sqrt{\int_{-h}^{h} \left(H(p_{1,x}+t) - \overline{\mathrm{H}}(p_{1,x})\right)^2 dt * \int_{-h}^{h} \left(H(p_{2,x}+t) - \overline{\mathrm{H}}(p_{2,x})\right)^2 dt}} \quad (1)$$

$$\overline{\mathrm{H}}(p_{i,x}) = \frac{1}{2h} \int_{-h}^{h} \overline{\mathrm{H}}(p_{i,x}+t) dt \quad (2)$$

$$H(p_{2,x}) = p(x) * H(p_{1,x}) + a(x) \quad (3)$$

H is the magnetic field strength in ampere per meter [A/m]

h is the centering length in [m]

$p_{1,2}$ is the proportionality factor, it describes the strength of the magnetic field for $p_2 > p_1$

a is the constant.

For the example stray field measurements 1 (8 A) and 3 (4 A) were used to calculate the correlation coefficient r which is shown in Fig. 4, the proportionality factor p shown in Fig. 5 and the constant as shown in Fig. 6.

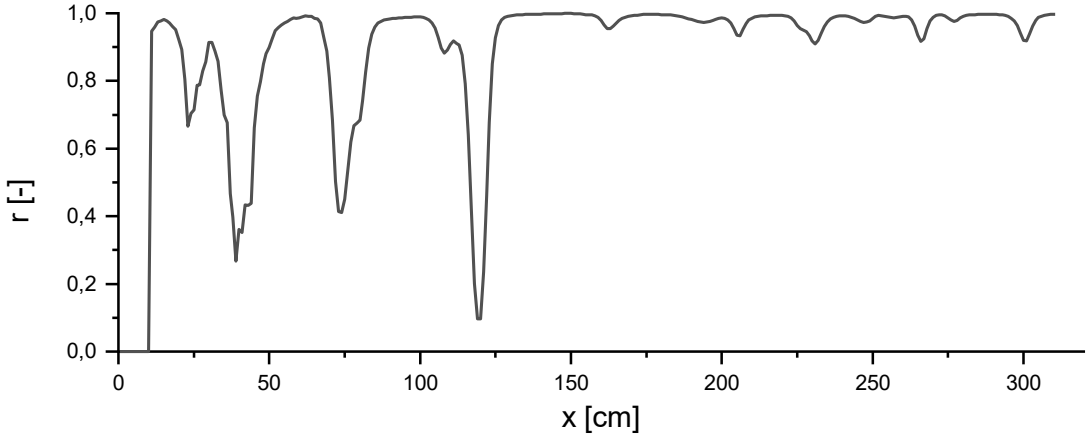

Fig. 4: Correlation factor r between stray field measurements 1 (8 A) and 3 (4 A). No indication of a fracture

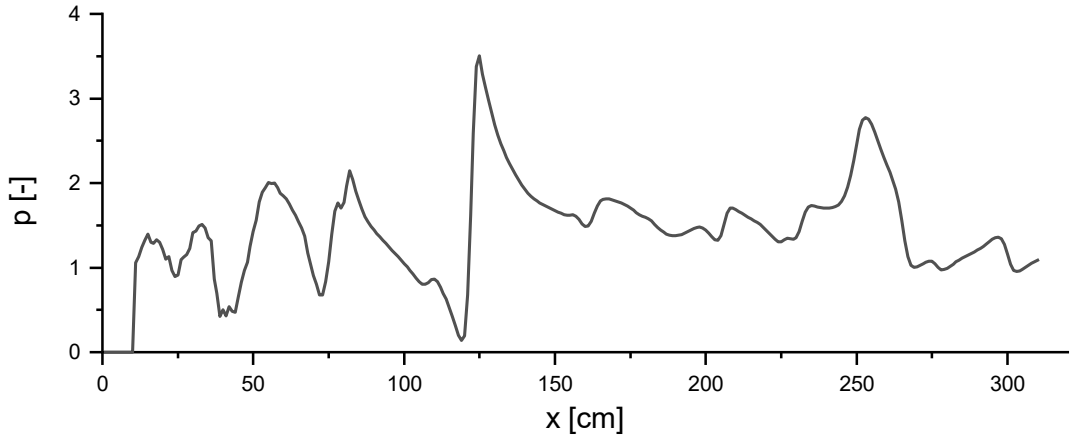

Fig. 5: Proportionality factor p stray field measurements 1 (8 A) and 3 (4 A). No indication of a fracture

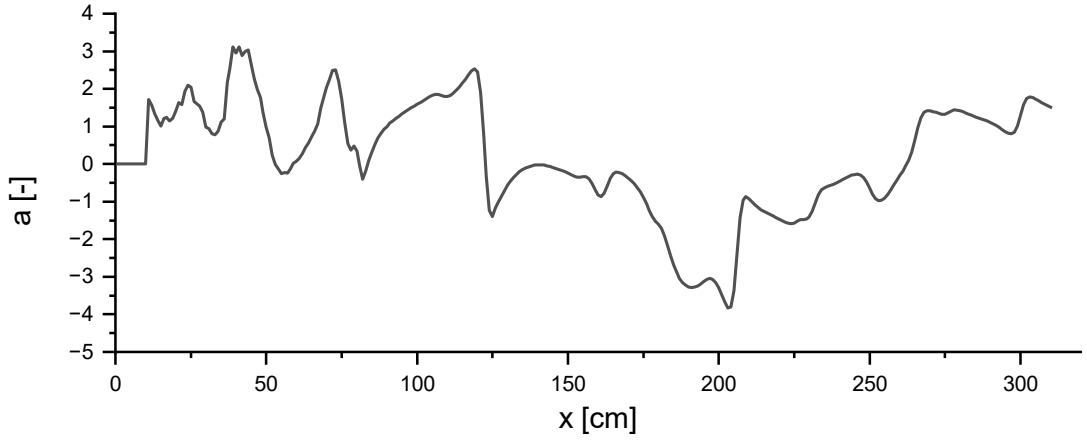

Fig. 6: Constant a stray field measurement 1 (8 A) and 3 (4 A). Indication of a fracture

3.2 Difference of active stray field measurements

The difference of two active stray field measurements is based on the same ferromagnetic material properties as the similarity function. When subtracting the magnetic field at a lower magnetization from a field at a higher magnetization, only the fracture signal should remain. To further suppress the magnetic signals of the rebars, the average value of p is calculated from equation (3) and the weaker magnetic field is divided by it. The result of equation (4) is exemplified in Fig. 7.

$$H_{p2-p1} = H_{p2} - \frac{H_{p1}}{p_{mean}} \tag{4}$$

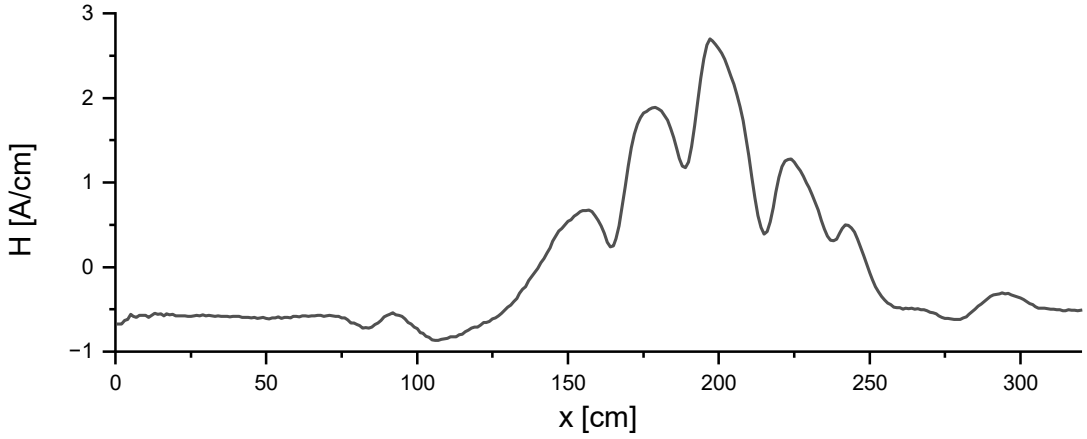

Fig. 7: Difference of active stray field measurements 1 (8 A) and 3 (4 A). Fracture becomes visible

3.3 Addition of residual field measurements

After the magnetization process is completed with active stray field measurements, the first residual field is measured. At this point, the residual magnetization of the stirrups is as low as possible, and the magnetization of the prestressing steel is as high as possible. Before measuring the second residual field, the polarization of the stirrups is inverted. By adding the two residual field measurements, the stirrup signals are significantly reduced or even eliminated. At the same time, the fracture signals are duplicated, and their amplitude doubled. This can be seen in Fig. 8.

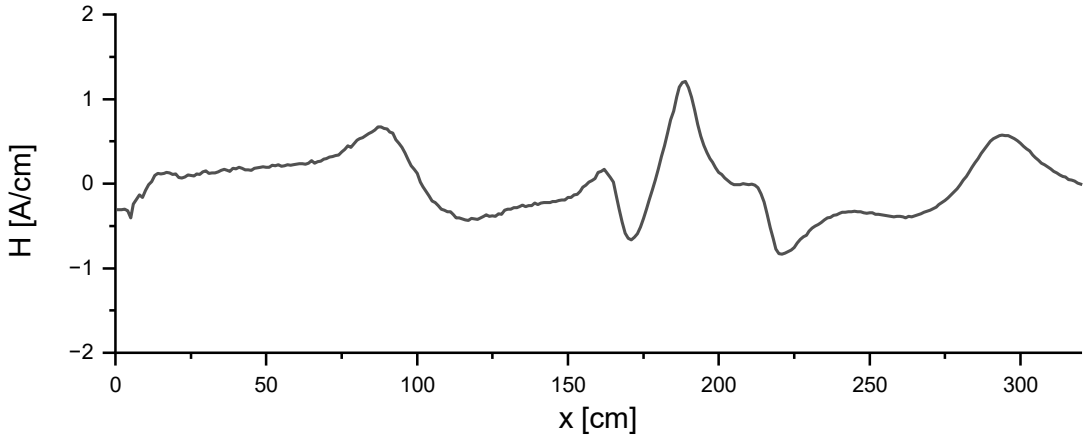

Fig. 8: Addition of residual field measurements 1 (2 A) and 2 (-2 A). Fracture, start and end of prestressing steel become visible

3.4 Stirrup correction

In addition to the methods based on the use of distinct stages of the magnetization process, analytical equations have been developed. In this step, the stirrups are cleaned from the measured residual fields. This is possible because the superposition principle applies to residual field measurements, which is unfortunately not the case for active stray field measurements. First, the exact position of the stirrups can be determined from the residual field measurement. The position of the stirrup shows an inflection point in the magnetization curve. At these locations (x_B) an idealized stirrup signal (5) is placed. z_B denotes an empirical parameter, depending on the concrete cover of the rebars.

$$H_B(x) = p_n \frac{1000 * (x - x_B)}{[(x - x_B)^2 + {z_B}^2\,]^{\frac{5}{2}}} \tag{5}$$

The idealized signal is fitted with equation (6) using the best-fit-method. Solving the linear system of equation calculates the parameter p_n, which is used to clean the residual field H_m.

$$\int \left[\frac{d}{dx} H_m(x) - \sum_{n=1}^{N} p_n * \frac{d}{dx} H_{B,n}(x) \right] * \frac{d}{dx} H_B(x) dx = 0 \tag{6}$$

After subtracting the fitted stirrup signal the cleaned signal H_R remains (7). Which is shown by way of example in Fig. 9.

$$H_R(x) = H_m(x) - \sum_{n=1}^{N} p_n * H_B \tag{7}$$

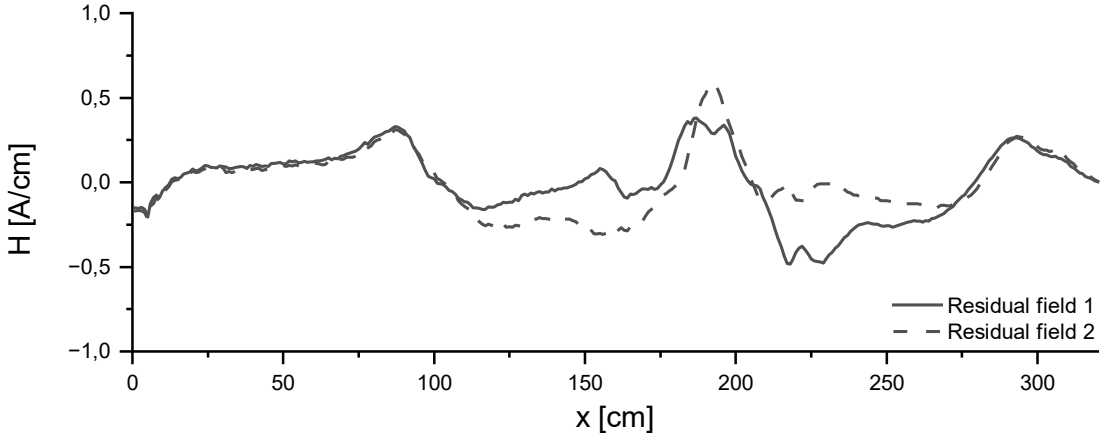

Fig. 9: Stirrup correction of residual field measurements 1 (2 A) and 2 (-2 A) with z_B=3 Fracture, start and end of prestressing steel become visible

3.5 Addition of residual field measurements with stirrup correction

The addition of residual field measurements with stirrup correction is the combination of the above two methods. It needs to be mentioned because it is one of the most effective algorithms for suppressing the signals of the stirrups. First the stirrups are removed with the analytical equations and secondly the two residual fields with stirrup correction are added. In the example the two corrected residual fields in Fig. 9 are added and the result is given in Fig. 10.

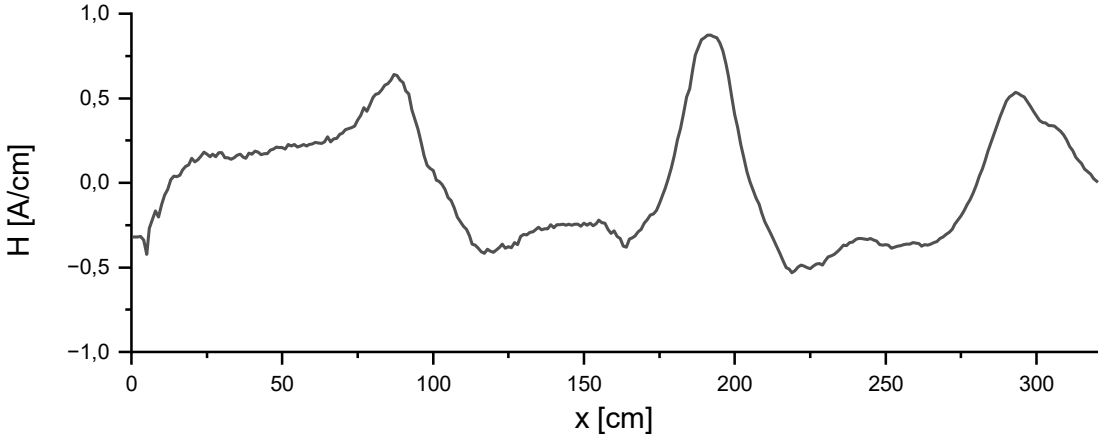

Fig. 10: Addition of corrected residual field measurements 1 (2 A) and 2 (-2 A) with z_B=3 Fracture, start and end of prestressing steel become visible

3.6 Correlation with fracture signal

After suppressing the stirrups as far as possible with one of the methods described above, they are evaluated by means of local correlation with a typical fracture signal. The process of correlating a measurement with the idealized fracture signal can be repeated with each step of the filtering process and the raw data. For this example, the correlation with the difference of the active stray field measurements and the addition of the corrected residual field measurements are shown. Equation (8) calculates the magnetization of the idealised fracture signal H_f. x_0 is the assumed location of the fracture and z_0 is the distance of the probe.

$$H_f(x) = \frac{p_f(x_0)}{[(x - x_0)^2 + z_0^2]^{\frac{3}{2}}} \tag{8}$$

The fracture amplitude p_f is a fitting parameter to the Signal H with equation (9). The results for the example are illustrated in Fig. 11 for the addition of corrected residual field measurements.

$$p_f(x) = \frac{\int_{-h}^{h} H(x+t) * H_f(t)dt - 2 * \overline{\mathrm{H}} - \overline{\mathrm{H}}_f}{\int_{-h}^{h} H_f^2(t) - 2 * h * \overline{\mathrm{H}}_f{}^2} \tag{9}$$

The local correlation coefficient r_f describes the similarity of the signal H with a typical fracture signal H_f. It is calculated with equation (10), (11) and (12) and the results for the example are shown in Fig. 12 for the addition of corrected residual field measurements.

$$r_f(x) = \frac{\int_{-h}^{h}\left(H(x+t) * H_f(x+t) - \overline{\mathrm{H}}_f(x) * \overline{\mathrm{H}}\right)dt}{\int_{-h}^{h}\left(H(x+t) - \overline{\mathrm{H}}(x)\right)^2 dt * \int_{-h}^{h}\left(H_f(x+t) - \overline{\mathrm{H}}_f(x)\right)^2 dt} \tag{10}$$

$$\overline{\mathrm{H}}(x) = \frac{1}{2h}\int_{-h}^{h} H(x+t)dt \tag{11}$$

$$\overline{\mathrm{H}}_{Br}(x) = \frac{1}{2h}\int_{-h}^{h} H_{Br}(x+t)dt \tag{12}$$

At every point x of the measurement the local correlation r_f and p_f are combined and filtered. In the last step only r_f values above a set threshold are considered. This value is often set to r_S=0.7 (13).

$$r_f(x) \geq r_S \tag{13}$$

By multiplying the local correlation r_f and the fracture amplitude p_f a weighted fracture amplitude P_I(x) is obtained. Which is illustrated in Fig. 13.

$$P_I(x) = r_f(x) * p_f(x) \tag{14}$$

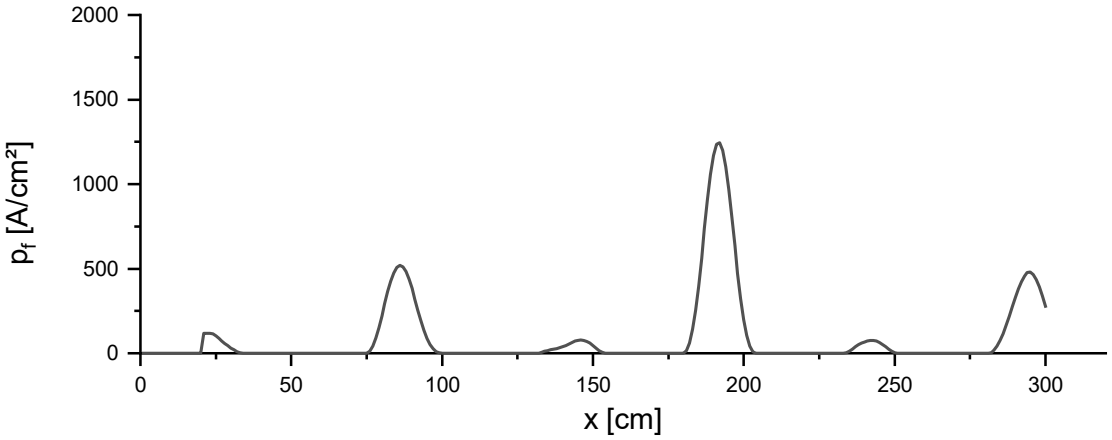

Fig. 11: Fracture amplitude p_f of addition of corrected residual field measurements 1 (2 A) and 2 (-2 A) with z_B=3

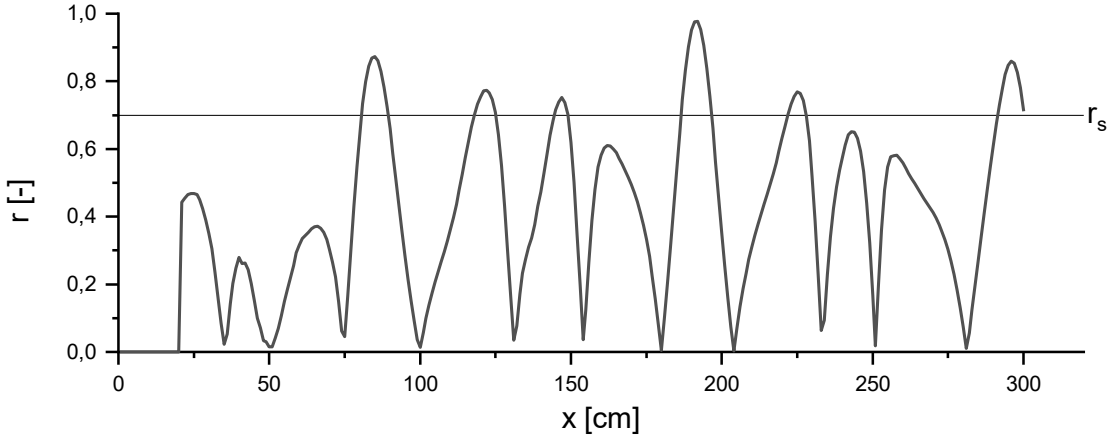

Fig. 12: Correlation coefficient r between addition of corrected residual field measurements 1 (2 A) and 2 (-2 A) with z_B=3 and idealized fracture signal

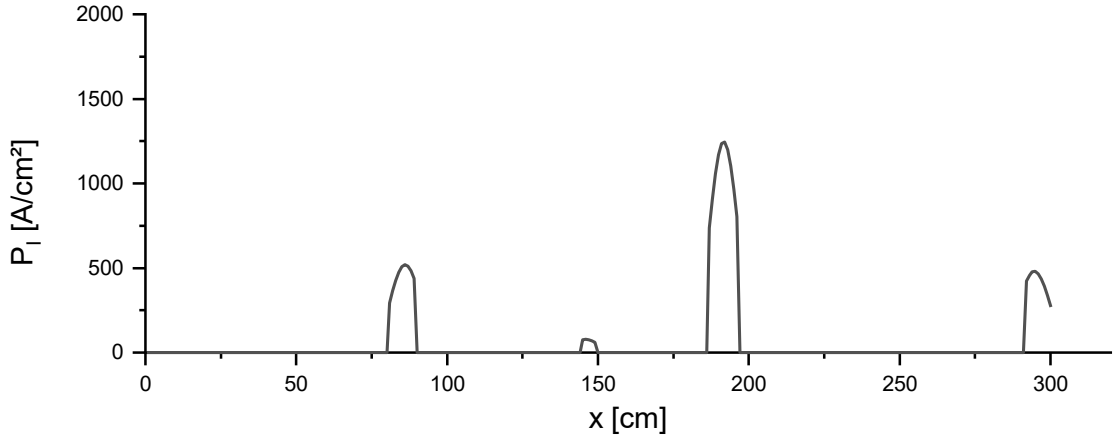

Fig. 13: Weighted fracture amplitude P_I of addition of corrected residual field measurements 1 (2 A) and 2 (-2 A) with z_B=3
Fracture, start and end of prestressing steel are clearly visible

4. TARGET OF STUDY

The target of the study is to evaluate the described algorithms for suppression of reinforcement signals and detection of fractures. This does not mean that the experimental setup can show how effective the algorithms are. It is a simplified version of a real scenario in order to study the equations and the underlying assumptions in as much detail as possible.

The main focus was placed on studying the input parameters z_0 (depth of the prestressing steel) and z_B (depth of the rebars). They influence the shape of the idealized fracture and rebar signals. Another objective was to evaluate the interactions between the rebar signals in the residual field measurements. It was important to verify that the Superposition principle applies. Furthermore, the linear system of equations resulting from (6) were reviewed to see if they adequately describe the magnetic interaction of the rebars.

5. EXPERIMENTAL SETUP

To achieve the objective of the study, the experimental setup was as simple as possible. A bar of prestressing steel type Sigma oval (St 145/160) was sawn into two parts. It was then glued to laminated timber with a fracture width of 1 mm. The specimen was two meters long, which means that the beginning and the end are visible during the measurements. It is expected that a fracture-like signal can be seen at these points.

To investigate the influence of reinforcing bars, five holes were drilled in the laminated timber. One hole was located directly under the fracture of the prestressing steel, two holes at a distance of 25 cm and two more at a distance of 50 cm. The position of three identical bars was varied during the experiments. Each bar had a length of 86 cm, a diameter of 16 mm and was made of B500B reinforcing steel. This setup is shown in Fig. 14.

An even simpler experimental setup is given in Fig. 15. The reinforcing bars without prestressing steel were placed on a wooden board and fixed in such a way that the magnet does not change their position.

Fig. 14: Experimental setup- fractured prestressing steel with varying positions and combinations of rebars

Fig. 15: Experimental setup - different positions and combinations of rebars

6. EXPERIMENTAL PROCEDURE

Two geometrical influencing factors have been varied, the probe distance and the positions of the rebars. The different probe distances are summarized in Table 1. The start of the prestressing steel was constantly at 90 cm, the rupture at 190 cm and the end of the prestressing steel at 290 cm. Table 2 shows the rebar positions which were investigated for all probe distances. Table 3 shows additional rebar positions which were investigated only for z_0=10 cm and z_B=4.2 cm. Table 4 lists

the probe distance z_B and the reinforcement positions that were studied without prestressing steel.

Table 1: Investigated probe distances to z_0 (prestressing steel) and z_B (rebar)

$z_{0,\,m}$ [cm]	$z_{B,\,m}$ [cm]
10.0	4.2
12.0	6.2
13.8	8.0
14.9	9.1
19.9	14.1

Table 2: Investigated rebar positions for all probe distances

Arrangement number	Position Rebar 1 [cm]	Position Rebar 2 [cm]	Position Rebar 3 [cm]
1	0	0	0
2	0	190	0
3	165	190	215
4	165	190	0
5	0	190	215
6	165	0	0
7	0	0	215
8	165	0	215

Table 3: Additional investigated rebar positions only for Z_0=10 and Z_B=4.2

Arrangement number	Position Rebar 1 [cm]	Position Rebar 2 [cm]	Position Rebar 3 [cm]
9	140	190	240
10	140	0	0
11	0	0	240
12	140	0	240

Table 4: Investigated rebar positions without prestressing steel

z_B [cm]	Position Rebar 1 [cm]	Position Rebar 2 [cm]	Position Rebar 3 [cm]
7	0	180	0
7	155	180	205
7	130	180	230
8,9	0	180	0
8,9	155	180	205
8,9	130	180	230
13,6	0	180	0
13,6	155	180	205

7. RESULTS

First, the idealized signals are compared with the measured signals. They are adjusted by varying the parameters by hand. In this way, not only the equations but also the underlying assumptions can be examined and verified.

7.1 Comparison of the idealized and measured signals

The two main formulas used to describe the magnetic field emanating from the specimen are the fracture signal and the stirrup signal. The stirrup signal is also considered when multiple rebars are present.

7.1.1 Fracture signal

An excerpt of the measured fracture signals without rebars and their corresponding idealized signals are given in Fig. 16. In a first step the depth parameter z_0 was chosen to be equal to the real probe distance. Only for $z_{0,m}$ = 10 cm the fit could be improved by varying the parameter z_0. In general, the formula for the fracture signal adequately describes the real magnetic behaviour of the prestressing steel fracture.

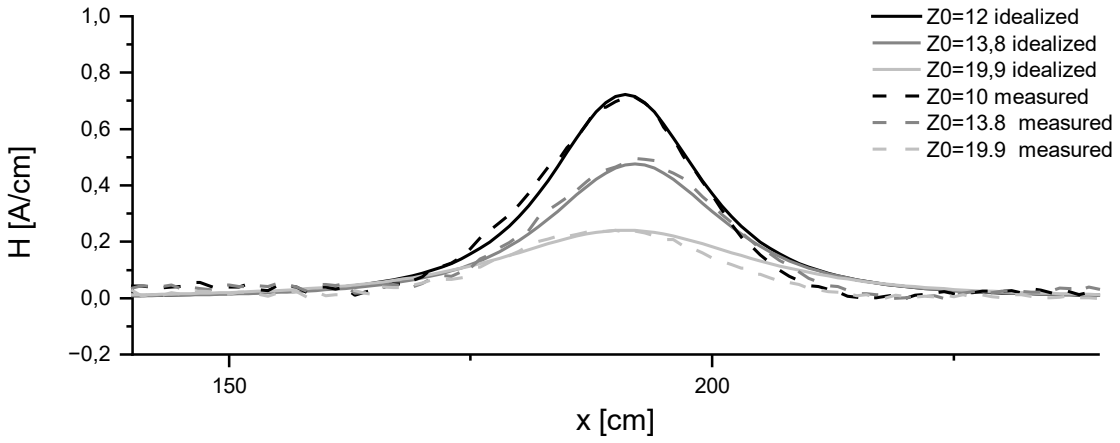

Fig. 16: Comparison between idealized fracture signals and measured signals in residual field 1 at $z_{0,m}$=10 cm with z_0=12 cm (p_f=1250), $z_{0,m}$=13.8 cm with z_0=13.8 cm (p_f=1250) and $z_{0,m}$=19.9 cm with z_0=19.9 cm (p_f=1900)

Table 5 shows all of the measurements for the probe distances $z_{0,\,m}$ = 10 cm, 12 cm, 13.8 cm, 14.9 cm and 19.9 cm. The parameter z_0 was again equal to the probe distance $z_{0,m}$. After the fitting with p_f the correlation coefficient r is consistently greater than 0.95. It is important to note that the manual fitting was done

using a constant p_f while the algorithmic fitting uses a fitting vector. The highest value of the vector p_f is given in the table below.

Table 5: p_f and r_f for measurements without rebars with z_0 equal to real probe distance $z_{0,m}$

Measure-ment	Probe distance	$z_{0,m} = 10$	$z_{0,m} = 12$	$z_{0,m} = 13.8$	$z_{0,m} = 14.9$	$z_{0,m} = 19.9$
SF1	p_f	632	844	947	1161	1876
	r_f	0.991	0.976	0.970	0.957	0.986
SF2	p_f	728	916	1073	1320	2156
	r_f	0.989	0.971	0.957	0.958	0.994
SF3	p_f	866	1078	1309	1640	2448
	r_f	0.976	0.965	0.980	0.986	0.993
SF4	p_f	959	1254	1507	1728	2478
	r_f	0.976	0.991	0.995	0.994	0.994
RF1	p_f	691	1058	1376	1654	2497
	r_f	0.983	0.992	0.996	0.997	0.997
RF2	p_f	706	1089	1384	1620	2573
	r_f	0.988	0.995	0.996	0.997	0.997

Increasing the parameter z_0 flattens the fracture signal. By fitting the flatter signal to the measurement, higher fracture amplitudes p_f are obtained. When comparing signals from different probe distances, it is useful to normalize the fracture amplitude to $z_0 = 10$. Table 6 shows that the parameter p_f decreases almost proportional to the magnetic field strength H as the probe distance increases, which can be compared with Fig. 16. The correlation coefficient decreases slightly for larger probe distances but is still sufficient for the requirements of this setup.

Table 6: p_f and r_f for measurements without rebars with $z_0 = 10$

Measure-ment	Probe distance	$z_{0,m} = 10$	$z_{0,m} = 12$	$z_{0,m} = 13.8$	$z_{0,m} = 14.9$	$z_{0,m} = 19.9$
SF1	pf	632	473	328	311	163
	rf	0.991	0.979	0.976	0.968	0.970
SF2	pf	728	513	375	353	182
	rf	0.989	0.979	0.965	0.967	0.971
SF3	pf	866	608	453	435	207
	rf	0.976	0.972	0.982	0.989	0.966
SF4	pf	959	690	508	444	209
	rf	0.976	0.988	0.985	0.983	0.960
RF1	pf	691	570	453	414	203
	rf	0.983	0.980	0.975	0.975	0.954
RF2	pf	706	589	457	407	214
	rf	0.988	0.984	0.976	0.975	0.960

7.1.2 Stirrup signal

The measured signals of single rebars without prestressing steel and their corresponding ideal signals are given in Fig. 17. The parameter z_B was set equal to the real probe distance and p_1 was fitted by hand. Overall, the magnetic behaviour is adequately represented by the fitted ideal rebar signals.

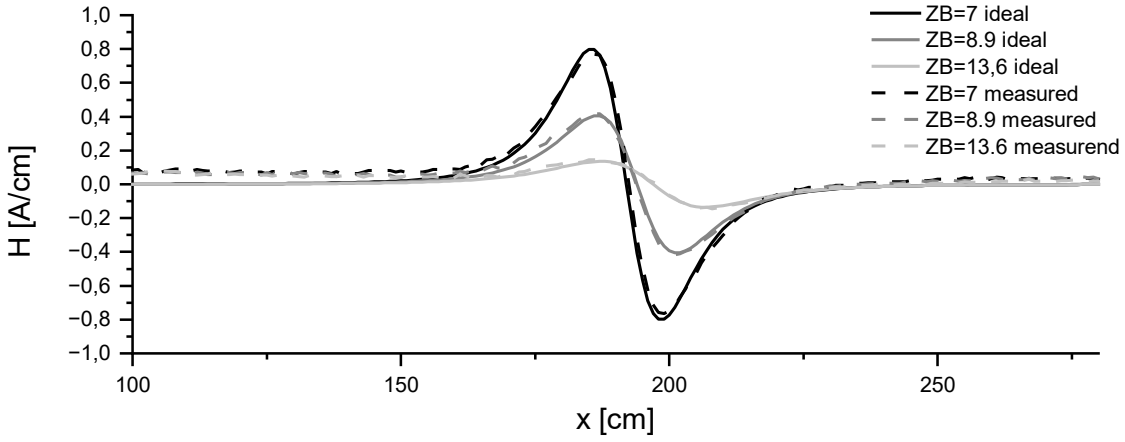

Fig. 17: Comparison between idealized stirrup signals and measured signals in residual field 1 at z_B=7 cm (p_1=80), z_B=8.9 cm (p_1=70) and z_B=13.6 cm (p_1=70)

To evaluate the assumption that the superposition principle applies to residual field measurements, experiments with multiple rebars were performed. Fig. 17 already shows that the idealized rebar signal adequately describes the magnetic field of a single rebar. Fig. 18 shows the same probe distances with two additional rebars in a distance of 25 cm. The idealized signals were fit by hand, using equation (5). The parameter p_n was estimated and incrementally adapted. The results

of the fitting show that the superposition principle applies to residual field measurements and that the formulas adequately describe the magnetic field behaviour.

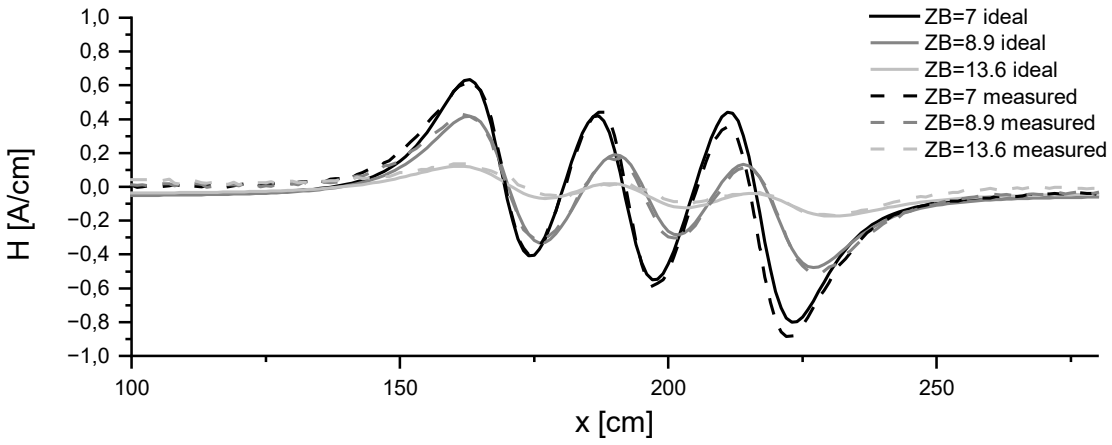

Fig. 18: Comparison between idealized stirrup signals and measured signals in residual field 1 at z_B=7 cm (p_1=62, p_2=62, p_3=62), z_B=8.9 cm (p_1=75, p_2=63, p_3=70) and z_B=13.6 cm (p_1=70, p_2=70, p_3=70)

7.2 Detection of fractures with the application of the algorithms

The goal of the algorithms is to suppress interference signals from the rebars and make the fracture signals as clear as possible. That's why almost all the experiments were performed with a fracture present. The interference suppression algorithms are evaluated in conjunction with the correlation of the fracture signal. 44 different setups with varying rebar arrangements and probe distances were investigated. The comparison of Table 6 and Table 5 shows that the fracture amplitude is increasing when z_0 is increased. To estimate the impact of influencing factors the fracture amplitudes is normalized to $z_0 = 10$.

It was important to investigate the influence of the probe distance and the different reinforcement arrangements. For this reason, box plots were created taking into account these influencing factors. In addition to the strength of the fracture amplitudes, false positives are also critical to the evaluation of an algorithm. False positives are fracture amplitudes at locations where no fracture was installed. To provide a more comprehensive overview of the quality of the results, the highest false positive value is also shown in a separate figure. The beginning and end of the prestressing steel were not counted as false positives because a fracture amplitude at the end of a bar parallel to the measurement direction is expected and does not occur in real constructions.

To ensure clear presentation the additional rebar arrangements from Table 3 were added in the same graph as the other rebar arrangements from Table 2. However, it is important to note that these rebar arrangements were only tested for one probe distance. If there is no box visible in a figure, all the fracture amplitudes were zero and the fractures were not found.

7.2.1 Similarity function of active stray field measurements

The similarity function is the only algorithm that is not evaluated using the correlation with the fracture signal. It is difficult to objectively evaluate the results of the similarity function because the graphs show relative changes. Therefore, all results were considered individually and judged whether there was a clear indication of fracture or not. If there was a clear indication of fracture at the correct location, with no false positives at other locations, the fracture was considered to be found.

The aim was to find out which parameter (correlation coefficient r, proportionality factor p or constant a) gives the most consistent results and which combination of stray fields is most suitable for comparison. All possible combinations are listed in Table 7.

Table 7: Possible stray field combinations

Stronger stray field p2	**Weaker stray field p1**
Stray field 1 (8 A)	Stray field 2 (6 A)
Stray field 1 (8 A)	Stray field 3 (4 A)
Stray field 1 (8 A)	Stray field 4 (2 A)
Stray field 2 (6 A)	Stray field 3 (4 A)
Stray field 2 (6 A)	Stray field 4 (2 A)
Stray field 3 (4 A)	Stray field 4 (2 A)

Table 8 shows the results of the evaluation as to what percentage of the category was counted as found. Considering all stray field combinations, the most effective parameter in this setup was the constant a, 70 % of the combinations were count as found. For the correlation coefficient r only 3 % and proportionality factor p only 8 % were positive. That's why only the constant a is considered in the following analysis. The best stray field combinations were SF 1 (8 A) - SF 4 (2 A), SF 2 (6 A) - SF 4 (2 A) and SF 3 (4 A) - SF 4 (2 A). It is noticeable that the weaker stray field p_2 was always stray field 4 (2 A).

Table 8: Results of the evaluation of the different parameters (correlation coefficient r, proportionality factor p or constant a) and stray field combinations

Stray field (SF) p2	Stray field (SF) p1	Parameter	Percentage found
SF 1 (8 A)	SF 2 (6 A)	r	2 %
		p	2 %
		a	48 %
SF 1 (8 A)	SF 3 (4 A)	r	2 %
		p	5 %
		a	73 %
SF 1 (8 A)	SF 4 (2 A)	r	2 %
		p	14 %
		a	80 %
SF 2 (6 A)	SF 3 (4 A)	r	2 %
		p	2 %
		a	57 %
SF 2 (6 A)	SF 4 (2 A)	r	2 %
		p	14 %
		a	82 %
SF 3 (4 A)	SF 4 (2 A)	r	7 %
		p	9 %
		a	80 %

Probe spacing had no effect on the results. The influence of the different rebar arrangements was decisive. Rebar arrangement 1 from Table 2, where no rebar was present, was never found. Reinforcement arrangements 2 to 8 all indicated a fracture at the correct location. Of the additional rebar arrangements from Table 3, only arrangement number 9 was found. 10, 11 and 12 were counted as not found.

7.2.2 Difference of active stray field measurements

In addition to evaluating the influencing factors it was also an aim to find the most promising combination of stray fields for comparison. All combinations are listed in Table 7. In order to limit the number of tables in this chapter, only one example is shown: Table 9 shows the results for the difference of active stray field measurements 2 (6 A) and 4 (2 A). The influencing factors probe distance and rebar arrangement are considered.

Table 9: Median of weighted fracture amplitudes P_1 at right and false locations of the difference of active stray field measurements 2 (6 A) and 4 (2 A) considering probe distance z_0 and rebar arrangement

Probe distance z_0 [cm]	Right location Median [A/cm²]	False location Median [A/cm²]
10	741	773
12	1578	773
13.8	1064	420
14.9	632	395
19.9	345	172

Arrangement number	Right location Median [A/cm²]	False location Median [A/cm²]
1	155	73
2	1017	61
3	910	389
4	1268	401
5	1469	291
6	942	1248
7	1958	1149
8	225	711
9	540	639
10	325	1604
11	410	2177
12	536	926

7.2.3 Addition of residual field measurements

Table 10 shows the results of the weighted fracture amplitude P_I of the addition of residual field measurements. The influencing factors probe distance and rebar arrangement are considered.

Table 10: Median of weighted fracture amplitudes P_I at right and false locations of addition of residual field measurements 1 (2 A) and 2 (-2 A) considering probe distance z_0 and rebar arrangement

Probe distance z_0 [cm]	Right location Median [A/cm²]	False location Median [A/cm²]
10	1422	529
12	1177	227
13.8	1008	219
14.9	820	172
19.9	406	81

Arrange-ment number	Right location Median [A/cm²]	False location Median [A/cm²]
1	912	51
2	1040	43
3	1068	341
4	1068	339
5	989	99
6	1028	389
7	874	87
8	959	345
9	1387	734
10	1325	594
11	1345	815
12	1295	817

7.2.4 Stirrup correction

One way to evaluate the stirrup correction is the evaluation of the remaining signal after subtracting the stirrup signal. In an ideal case only the fracture amplitudes without false positive should remain. At the same time, the fracture amplitudes should not be reduced by the stirrup correction. Table 11 shows the results of the weighted fracture amplitude P_I of the corrected residual field measurement 2.

Table 11: Median of weighted fracture amplitudes P_I at right and false locations of corrected residual field measurements 2 (-2 A) considering probe distance z_0 and rebar arrangement

Probe distance z_0 [cm]	Right location Median [A/cm²]	False location Median [A/cm²]
10	649	60
12	549	47
13.8	442	38
14.9	356	30
19.9	169	18

Arrange-ment number	Right location Median [A/cm²]	False location Median [A/cm²]
1	263	22
2	529	25
3	503	53
4	528	46
5	509	37
6	260	38
7	207	38
8	380	61
9	893	89
10	457	46
11	432	43
12	416	41

7.2.5 Addition of residual field measurements with stirrup correction

Table 12 shows the results of the weighted fracture amplitude P_I of addition of residual field measurements with stirrup correction. The influencing factors probe distance and rebar arrangement are considered.

Table 12: Median of weighted fracture amplitudes P_I at right and false locations of addition of residual field measurements with stirrup correction considering probe distance z_0 and rebar arrangement

Probe distance z_0 [cm]	Right location Median [A/cm²]	False location Median [A/cm²]
10	1108	99
12	938	75
13.8	678	54
14.9	540	67
19.9	269	36

Arrangement number	Right location Median [A/cm²]	False location Median [A/cm²]
1	529	41
2	721	42
3	679	80
4	736	84
5	737	62
6	529	64
7	447	35
8	774	104
9	1112	111
10	831	83
11	806	81
12	783	78

8. DISCUSSION AND SUMMARY

Magnetic flux leakage testing is a sophisticated non-destructive testing method. By analysing the measured magnetic fields, it can detect anomalies that may indicate fracture due to stress corrosion cracking, mechanical damage, fatigue or overload. This can provide valuable information as to the condition of the structure in question. Structures that are regularly inspected include prestressed concrete bridges, gymnasiums, assembly halls, schools, universities, stadiums and other long-span structures, some of which are heavily trafficked. The fracture behaviour of these structures can be sudden, brittle and low deformation. The structural condition of these structures is therefore undefined. Magnetic leakage field measurement can fill this knowledge gap, lead to the initiation of effective remediation measures and the prevention of dangerous structural damage up to the point of failure.

The results of the similarity function seem promising if the constant a is considered. Parameters p and r do not give clear indications for fracture in this setup. But even for constant a the additional rebar arrangement 9 to 12 which were further apart posed huge problems. This is an indication that rebar arrangements have decisive influence on the results. Further experiments in more realistic reinforcement arrangements are needed to validate the promising results of regarding constant a in the following stray field combinations: 1 (8 A) - 4 (2 A), 2 (6 A) - 4 (2 A) and 3 (4 A) - 4 (2 A). The probe distance up to 19.9 cm did not influence the results.

Fracture detection with the difference of active stray field measurements is definitively possible. The fracture amplitudes are generally higher than in residual field measurements and the probe distance has a less decisive role. Table 9 clearly shows that reinforcement arrangements have a huge impact on the results. Rebar arrangement 1, in which no reinforcement was present, low fracture amplitudes are registered. This is an indication that fracture signals are suppressed by the difference of active stray field measurements. The best results are obtained with rebar arrangements 2 to 5 in which a rebar was between the probe and the prestressing steel. In rebar arrangements 6 to 8 the rebars were located 25 cm adjacent to the fracture but not directly below it. This led to an increase in false positives. The rebar arrangements 9 to 12 where the rebars were 50 cm from the fracture. Only in arrangement 9 a rebar was between probe and fracture. These arrangements were only tested for the probe distance of 10 cm, but they still indicate that

the reinforcement governs the measured magnetic fields. If the difference of active stray field measurements is used for fracture detection, rebar arrangements must be considered. This is possible because rebar positions can be obtained from the residual field measurements and automatically presented while evaluating the active stray field measurements. It would still be desirable if more effective methods were developed to suppress the rebars.

The addition of residual field measurements in combination with correlation with the idealized fracture signal consistently shows higher fracture strengths than false positives. The strength of the fracture signal is almost linearly affected by the probe spacing. False positives show the same behaviour. Individual reinforcement arrangements have no effect on the fracture amplitudes. Table 10 indicates that some arrangements lead to slightly stronger false positives, which are still weaker than the fracture amplitudes.

Suppressing the rebar signals analytically is quite effective for this setup. The rebar signal adequately describes the magnetic behaviour of rebars with transversal orientation and the principle of superposition applies. The strength of the fracture signal is influenced by the probe distance in an almost linear way. False positives are still present, but they are consistently low for alle probe distances and rebar arrangements (Table 11). This means that they can be filtered out by setting a threshold value. The results are consistent for corrected residual field measurements 1 and 2.

The addition of the corrected residual field measurements leads to high fracture amplitudes and consistently low false positives. The almost linear influence of the probe spacing is still visible while the false positives are not influenced by the probe spacing. The induvial rebar arrangements are successfully suppressed. The true fracture amplitudes are consistently greater than the false positives which means that they can be distinguished by setting a threshold (Table 12).

The algorithms for suppressing stirrup signals are generally more effective for residual field measurements than for active field measurements. There are several reasons for this result. First, the various steps of the magnetization process are designed to maximize the magnetization of prestressed steel that is parallel to the direction of the moving magnet and probe. At the same time, the magnetization of reinforcing bars that are transverse to the prestressed steel is minimized. The combination of the geometric arrangement and the magnetic material behaviour results in a low magnetic field of the rebars. The second reason is that the principle

of superposition applies to residual field measurements. Magnetic fields of different reinforcing elements can be added or subtracted and still adequately describe the magnetic behaviour. However, the comparison of Table 10 and Table 12 shows that the fracture amplitudes are reduced by about 30 % filtering out the rebars with the method described. In addition, the low number of false positives is an indication that there is still room for improvement.

REFERENCES

[1] SCHEEL, H.; HILLEMEIER, B.: *Ortung von Spannstahlbrüchen in metallischen Hüllrohren*. Abschlussbericht zum Forschungsauftrag des Deutschen Instituts für Bautechnik AZ.: IV 1-5-672/92, Berlin, 1996

[2] SAWADE; G.: *Forschungsbericht Förderkennzeichen 13 N 7249/3: Mobiles SQUID-Meßsystem zur Bauwerksinspektion Teilvorhaben Magnetisierungsvorrichtung und Signalverarbeitung*, Otto-Graf-Institut, Universität Stuttgart, Stuttgart, 2001

[3] RAMRATH, M.: *Quantitative Bewertung von magnetischen Streufeldsignalen mittels normierter Bruchamplituden*, Stuttgart: Universität Stuttgart, Institut für Werkstoffe im Bauwesen, 1998

[4] SAWADE, G.: *Prüfung von Spannbetonbauteilen mit magnetischen Methoden*, Beton- und Stahlbetonbau 105, Nr. Heft 3, pp. 154-164, 2010

[5] SAWADE, G., KRAUSE, H.J.: *Inspection of Prestressed Concrete Members using the Magnetic Leakage Flux Measurement Method – Estimation of Detection Limit,* Advances in Construction Materials 2007, pp. 639-649, 2007

[6] BOUSACK, H., SAWADE, G., KRAUSE, H.J.: *Patentschrift DE 196 31 490 C 2, Vorrichtung und Verfahren zur Unterdrückung von Signalen der Querbügel bei der Untersuchung von Spannbetonbauteilen mit der Methode der magnetischen Restfeldmessung,* 1998

[7] SAWADE; G.: *Forschungsbericht Nr: 13 N 6114 0: HTSL Squid in der Bauindustrie*, Otto-Graf-Institut, Universität Stuttgart, Stuttgart, 1996